Research Square

Preprints are preliminary reports that have not undergone peer review.
They should not be considered conclusive, used to inform clinical practice,
or referenced by the media as validated information.

Ba-Modified Bi4Ti3O12 Nanoparticles for Enhanced Electrochemical Energy Storage and Photocatalytic Methylene Blue (MB) Degradation

S. Sneka
Annamalai University
V. Ananthi
ananthi2312v@gmail.com

Annamalai University
G. Sivakumar
Annamalai University
S. Ramanathan
FEAT, Annamalai University

Research Article

Keywords: BBTO NPs, Co-precipitation method, diffusion-controlled process, Environmental application, Bode plot.

Posted Date: November 20th, 2026

DOI: https://doi.org/10.21203/rs.3.rs-11649151/v1

License: This work is licensed under a Creative Commons Attribution 4.0 International License.
Read Full License

Additional Declarations: No competing interests reported.

Ba-Modified $Bi_4Ti_3O_{12}$ Nanoparticles for Enhanced Electrochemical Energy Storage and Photocatalytic Methylene Blue (MB) Degradation

[a] S. Sneka, [b] V. Ananthi, [c] G. Sivakumar and [d] S.Ramanathan
[a] Research Scholar, Physics Department, Annamalai University, Tamilnadu 608 002, India
[b] Physics Section, FEAT, Annamalai University, Tamilnadu 608 002, India
On deputation to SSP College, Puthur, Tamilnadu 609 110, India
[c] Professor ,Department of Physics, Annamalai University, Tamilnadu 608 002, India
[d] Professor ,Department of Manufacturing Engg., Annamalai University, Tamilnadu 608 002, India
[b] Corresponding Author: E-mail: ananthi2312v@gmail.com

ABSTRACT

To study the effect of Ba-substitution on the morphological, optical, structural and electrochemical and photo catalytic properties of $Bi_4Ti_3O_{12}$ nanoparticles (NPs), the Ba-modified $Bi_4Ti_3O_{12}$ NPs were successfully synthesized. XPS, XRD and EDX confirmed the formation of bismuth titanate crystal structure and phase purity. Non-linear GCD profiles indicated that a pseudo capacitive charge-storage mechanism and electrochemical analysis demonstrated a significant dependence on a specific Ba concentration. The optimized BBTO-2 composition exhibited a maximum specific capacitance(Cs) of 691 Fg^{-1} at 1 Ag^{-1} due to improved interfacial ion-transport kinetics and reduced charge-transfer resistance, as demonstrated by electrochemical EIS and Bode analysis. Moreover, the optimized sample showed better catalytic activity toward the photo catalytic degradation of methylene blue (MB) under solar light irradiation with 87% degradation efficiency within 80 min. Results demonstrate that the controlled Ba modification can be utilized to synthesize the multifunctional $Bi_4Ti_3O_{12}$ NPs, applications in energy storage and environmental application.

Keyword

BBTO NPs, Co-precipitation method, diffusion-controlled process, Environmental application, Bode plot.

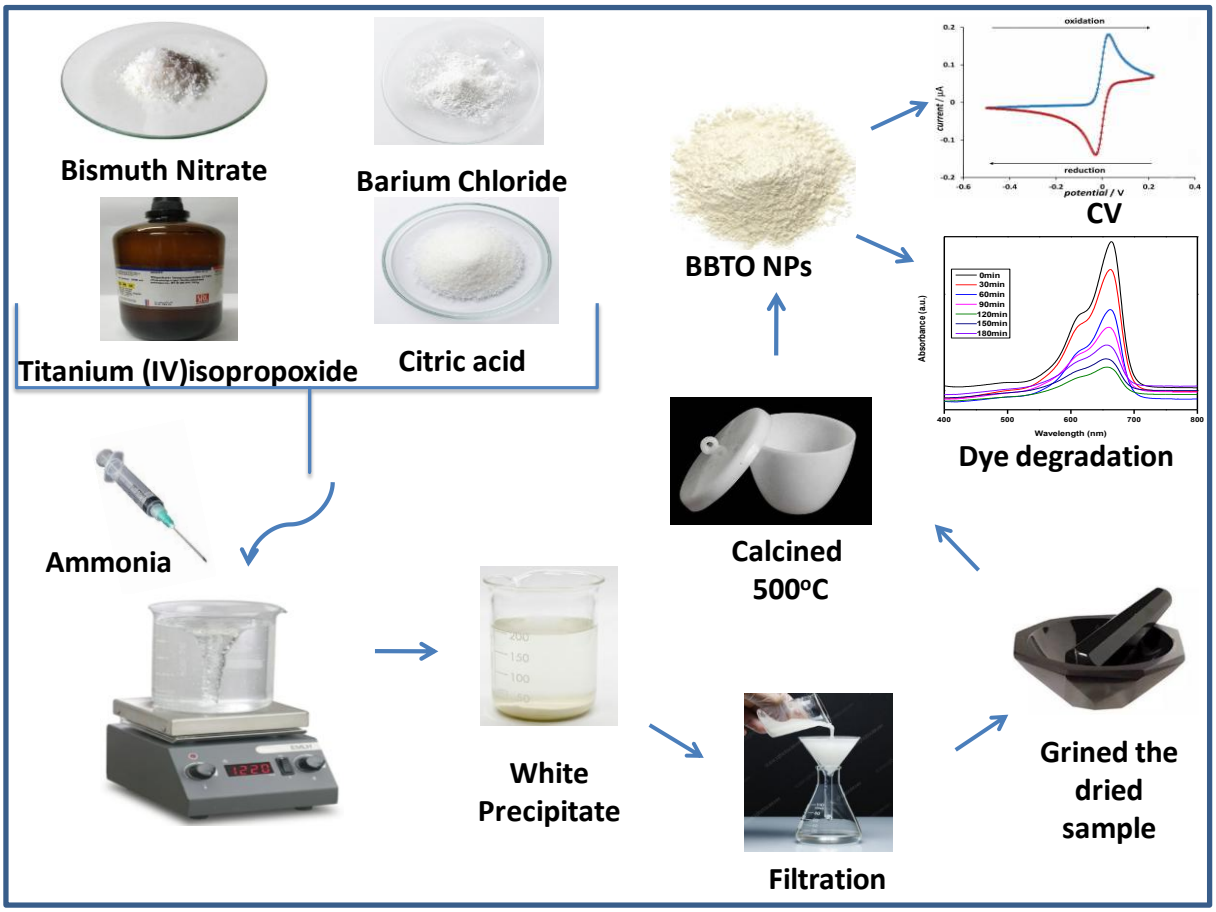

Fig.1 Graphical abstract

1. Introduction

Rapid population growth, industrialization and advancement in technology have increased the energy needs of the world, and at the same time improved the environmental pollution. The depletion of the conventional fossil fuel resources and corresponding environmental consequences have led to sustainable energy technologies and the energy storage systems. In this context, renewable energy sources solar and wind power provide viable alternatives to conventional energy sources, but their intermittent nature requires the development of energy storage technology. Simultaneously, the growing release of chemical pollutants from household and industrial activities [**1**] has led to a growing requirement for environmentally friendly wastewater-treatment technology.

Supercapacitor is a efficient electrical energy storage technology that can be used with conventional batteries due to its extended cycle life, high power density and rapid charge-discharge capability. Supercapacitor can charge and discharge energy quickly , indicating that they are more suitable for applications that require high power and frequent charge-discharge cycles. Conversely, batteries usually have higher energy density. They offer numerous advantages such as high power density, longer cycle life, rapid charging and discharging, wide operating temperature range, relatively low maintenance requirements, better security and environmental compliance. It still has low energy density compared to batteries, which is significant drawback for energy storage applications. Supercapacitor are therefore generally considered to be suitable for high power and short to moderate energy storage applications [**2**,**3**].

Sunlight, that provides a thousand times more energy per year to the earth surface than the world uses. Photocatalytic materials that use solar energy need to be developed to produce clean energy, synthesize renewable chemicals and reduce environmental pollutants [**4**]. Among all the studies conducted, photocatalysts has become a well trained technique for degradation of pollutants that is due to affordable and eco-friendly.

Most of the photocatalytic degradation studies are based on TiO_2 as the most used photocatalyst due to its high photocatalytic activity, superior stability, and nontoxicity [**5**]. However, TiO_2 can only absorb ultraviolet light and therefore cannot make full use of the sunlight, of which only 4-5% is visible solar energy. Meanwhile, the practical use of TiO_2 is limited because of the quick recombination of photogenerated electron-hole pairs [**6,7**]. Therefore, the development of visible-light-responsive photocatalysts has grown into a hot topic. Bismuth based materials are frequently employed by the scientists for photocatalytic degradation due to their low band gaps and significant photocatalytic activity under visible light. To enhance the photocatalytic activity, we examined the formation of heterojunctions between pure Bi_2O_3 and other semiconductors [**8,9**].

Multifunctional nanomaterials are of crucial significance for increasing the efficiency, selectivity of photocatalytic processes for the production of renewable chemicals, for the capture of clean energy, and for the development of sustainable catalytic pathways. Researchers are interested in modified TiO_2-based photocatalysts such as bismuth titanate due to their excellent optical and electrical properties [**10**]. Due to its unique electrical properties and crystal structure, bismuth titanate (BTO) has attracted the interest of researchers to investigate its catalytic properties.[**5**]. BTO has a layered Aurivilius structure is a structural intermediate in the binary Bi_2O_3–TiO_2 system. This structure is constructed by the stacked arrangement of $(Bi_2O_2)^{+2}$ tetraedrons and $(Bi_2Ti_3O_{10})^{-2}$ pseudo-perovskite layers. BTO is an interesting lead-free and eco-friendly material [**11,12**].

.

Many researchers have employed element doping [**13,14**], heterojunction formation by combination with semiconductors [**15,16**], morphology alteration [**17**], and other modification methods [**18-20**] to improve the catalytic and electrical performance. outlined is described an attempt has been made to enhance the specific capacitance of BTO by adding Ba as a reinforcing element, as supercapacitor have the potential for energy storage and environmental application, enhance the conductivity and improving the capacitive behaviour of BTO.

The synthesis and characterization in this work of $Bi_4Ti_3O_{12}$ compounds modified by Ba different substitutions to improve the electrochemical and photochemical properties. The effect of barium modification of bismuth titanate with the general formula $Bi_4Ti_{3-x}Ba_xO_{12}$ (X= 0.01, 0.02, 0.03) on the phase formation, morphological, electric and optical characteristics is discussed in the paper.

2.Exprimental section

2.1 preparation of BBTO NPs

The Co-precipitation method was used to synthesize BBTO NPs utilizing $Bi_4Ti_{3-x}Ba_xO_{12}$ (X= 0.01, 0.02, 0.03) with different barium doping concentrations. The sample was made by combining the nitrate salt source materials of 0.1M $[Bi(NO_3)_3.5H_2O]$ and (X= 0.01, 0.02, 0.03) $[Bacl_2.2H_2O]$. After being measured in a stoichiometric ratio, the precursors of the Bi and Ba salts were mixed with distilled water (DI) in a beaker. To create a uniform precursor mixture, the bismuth precursor solution was then progressively combined with a (X= 0.09, 0.08, 0.07) M titanium (IV) isopropoxide solution while being continuously stirred. An aqueous solution was prepared by mixing the chelating agent, citric acid ($C_6H_8O_7$), in a 0.2M ratio. Then the pH of the combined solution was adjusted to 11 by the addition of ammonia (NH_4OH) solution drop wise with stirring. The formation of white precipitate confirmed the successful synthesis of the precursor of BTO through co-precipitation process. The precipitate

obtained in this way was filtered and dried at 80°C for 3 h to remove any residual moisture. The dried product was grounded to a fine powder and calcined at 500 °C for 3 h to obtain crystalline BBTO NPs. The Ba-modified samples that were calcined (X= 0.01, 0.02, and 0.03) were referred to as BBTO-1, BBTO-2, and BBTO-3, respectively.

2.2 Electrochemical preparation of electrodes

Cyclic voltammograms of prepared electrode were obtained at varied scan rates from 5 to 100 mVs^{-1} in the potential range of 0 to 0.45 V. Chronopotentiometry was used to conduct the charge/discharge tests, with constant currents ranging from0 to 0.45 V (versus Ag/AgCl). Next, electrochemical impedance analysis was obtained in the 1Hz to 1MHz frequency range. Using the solvent N-methyl- 2-pyrrolidone to form a homogenous slurry, the working electrode preparation comprises of 80 wt% of active material, 10 wt% of PVDF powder, and 10 wt% of activated carbon, respectively. The mixture slurry was then applied to the surface on the nickel foil sheet current collector and slowly dried for 24 h at 80 °C. All tests were taken in an aqueous 1M KOH electrolyte with an electrode material prepared as a working electrode, Pt (platinum) wire as a counter electrode, and Ag/AgCl (silver/silver chloride) as a reference electrode in ambient conditions[**21**]. The electrochemical performance of the synthesized BTO NPs was tested using a Metrohm Autolab M204 electrochemical workstation paired with NOVA 2.1.4 software. The standard three-electrode setup was employed for cyclic voltammetry (CV), galvanostatic charge-discharge (GCD), and electrochemical impedance spectroscopy (EIS) studies.

From CV, GCD,

$$C_s = \frac{\int I\,V\,dV}{m \times s \times \Delta V} \qquad (1)$$

$$C_s = \frac{I\,dt}{m\Delta V} \qquad (2)$$

$$E = \frac{1}{2\times 3.6} C_s\,(\Delta V)^2 \qquad (3)$$

$$P = \frac{E\times 3600}{\Delta t} \qquad (4)$$

where the specific capacitance is denoted by Cs. GCD measurements are used to determine Cs in Eq. (1, 2), where I is the applied current A, Δt is the discharge duration s, m is the electrode mass g, and ΔV is the operational potential window V. Equations were also used to calculate the power density(P) W/kg and energy density (E) Wh/kg. (3) and (4) as mentioned.

2.3 Photo catalytic measurement

MB dye degradation under natural sun light to assess the photocatalytic activity of the produced BTO NPs. 0.01 g of MB dye was dissolved in 150 mL of DI water to create an aqueous MB solution. To achieve the same dispersion of the photocatalyst, 100 mL of the dye solution and 25 mg of BTO NPs were combined in a 250 mL beaker for each photocatalytic experiment. The mixture continually stirred using a magnetic stirrer. The suspension was maintained for the establishment of adsorption-desorption equilibrium between the dye molecules and the surface of catalyst, stirred before being exposed to sunlight.

After that, the photocatalytic degradation tests were conducted in direct sunlight. A UV-visible spectrophotometer operating in the 200–800 nm wavelength range was used to collect and evaluate aliquots of the reaction mixture at regular intervals of 30 minutes. The degradation process was measured by tracking the decline in the MB dye distinctive absorption peak. Using Eq. (4), the photocatalytic degradation efficiency (η) was determined[**22**].

$$Efficiency\ \eta\ (\%) = \left(1 - \frac{C}{C_o}\right) \times 100 \qquad (5)$$

where Co and C stand for the MB dye initial and residual concentrations prior to and following irradiation, respectively. A Shimadzu UV-1800 UV–Visible spectrophotometer was used to monitor the degradation of MB dye under sunlight irradiation in order to determine the samples photocatalytic degradation efficiency.

2.4 characterization

An X'Pert PRO diffractometer (PANalytical, Germany) with Cu Kα radiation (λ = 1.5406 Å) with operating conditions at 40 kV and 30 mA were utilized to analyze the crystal structure and phase composition by powder X-ray diffraction. Using scanning electron microscopy (SEM, JEOL JSM-5610LV), the surface appearance and elemental composition were examined. Using UV–Visible diffuse reflectance spectroscopy on a SHIMADZU UV-2600 spectrophotometer, the optical characteristics of the synthesized samples were examined. A PerkinElmer LS 45 fluorescence spectrophotometer was applied to determine the amount of photoluminescence in order to assess the charge-carrier recombination behavior. Using a Thermo Fisher Scientific device, X-ray photoelectron spectroscopy was used to investigate the chemical composition and oxidation states of the component elements.

3. RESULTS & DISSCUSSIONS

3.1.1 XRD analysis

XRD analysis used to confirm if Ba^{2+} was substituted into the $Bi_4Ti_3O_{12}$lattice. Figure **2**(a) shows the XRD patterns of Ba-substituted $Bi_4Ti_3O_{12}$with different Ba contents. The main phase of the substrate is $Bi_4Ti_3O_{12}$ (JCPDS No. 35-0795) and Ba(*) (JCPDS No. 842211), consisting of diffraction peaks $Bi_4Ti_{3-x}Ba_xO_{12}$, without any peak from the impurity phase. The (117) plane of $Bi_4Ti_3O_{12}$ phase is at 29°. The diffraction peaks are slightly shifted toward the lower value of 2θ with the increase of Ba^{2+} doping concentration Figure **2** (b). The spacing between the planes will expand when Bi^{3+} is partially substituted with Ba^{2+}, as the ionic radius of Ba^{2+} (1.35 Å) exceeds that of Bi^{3+} (1.03 Å). This modification can be explicated by the substitution of larger Ba^{2+} ions for Bi^{3+} within the $Bi_4Ti_3O_{12}$ lattice. In comparison to Bi^{3+}, Ba^{2+} possesses a larger ionic radius. Consequently, the interplanar distance increases when Ba^{2+} partially substitutes Bi^{3+}. According to Bragg law, the ensuing diffraction peak migrates toward diminished 2θ values as the interplanar spacing enlarges. Consequently, the detected peak shift signifies that Ba^{2+} has been integrated into the $Bi_4Ti_3O_{12}$ structure[**23]**.

The average crystallite size (D) was calculated using the Debye–Scherrer equation **[21**]

$$D = \frac{K\lambda}{\beta \cos\theta} \qquad (6)$$

where D is the average crystallite size (nm), (K) is the shape factor (0.9), (β) is the full width at half maximum (FWHM) (λ) is the X-ray wavelength of Cu Kα radiation (1.5406 Å) of the diffraction peak (in radians) and θ is the Bragg diffraction angle.

The specific surface area (SSA) was calculated using[**24**]

$$SSA = \frac{6000}{\rho D} \qquad (7)$$

Calculated crystallite size by Debye–Scherrer equation 18.16, 13.05, 27.83 nm. The calculated specific surface area (SSA) was 41.10, 57.18, 26.83 m^2 /g.

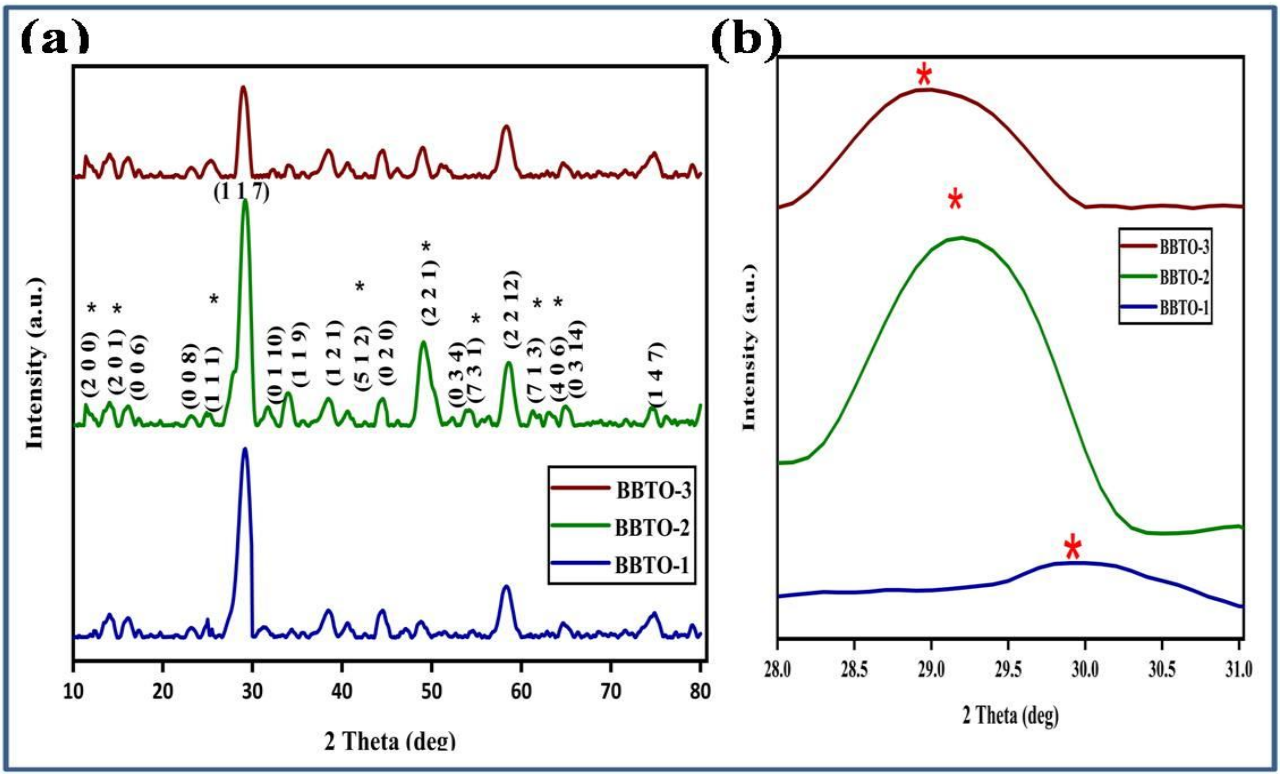

Fig. 2 (a, b)XRD patterns of BBTO NPs of (a) BBTO-1, (b) BBTO-2, (c) BBTO-3

3.1.2 SEM analysis

SEM micrograph of BBTO-1, BBTO-2 and BBTO-3 at 5µm magnification is shown in Figure **3**(a) Particles are in a pattern of interconnected clusters which makes it look disorganized and clustered morphology. Figure **3**(b), where the mainstructures have a granular texture and sharp faceted edges. Figure **3**(c) reveals a rough, highly textured surface composed of densely packed, hierarchical complexes and agglomerates. Such porous agglomerates and rough surface features imply a surface area-to-volume ratio which is useful for applications such as catalysis and energy storage [**25**]. The micrographs show a material of irregular shape. The EDX spectra corresponded with the presence of Bi, Ba, Ti and O, which demonstrated the high purity of BBTO NPs.

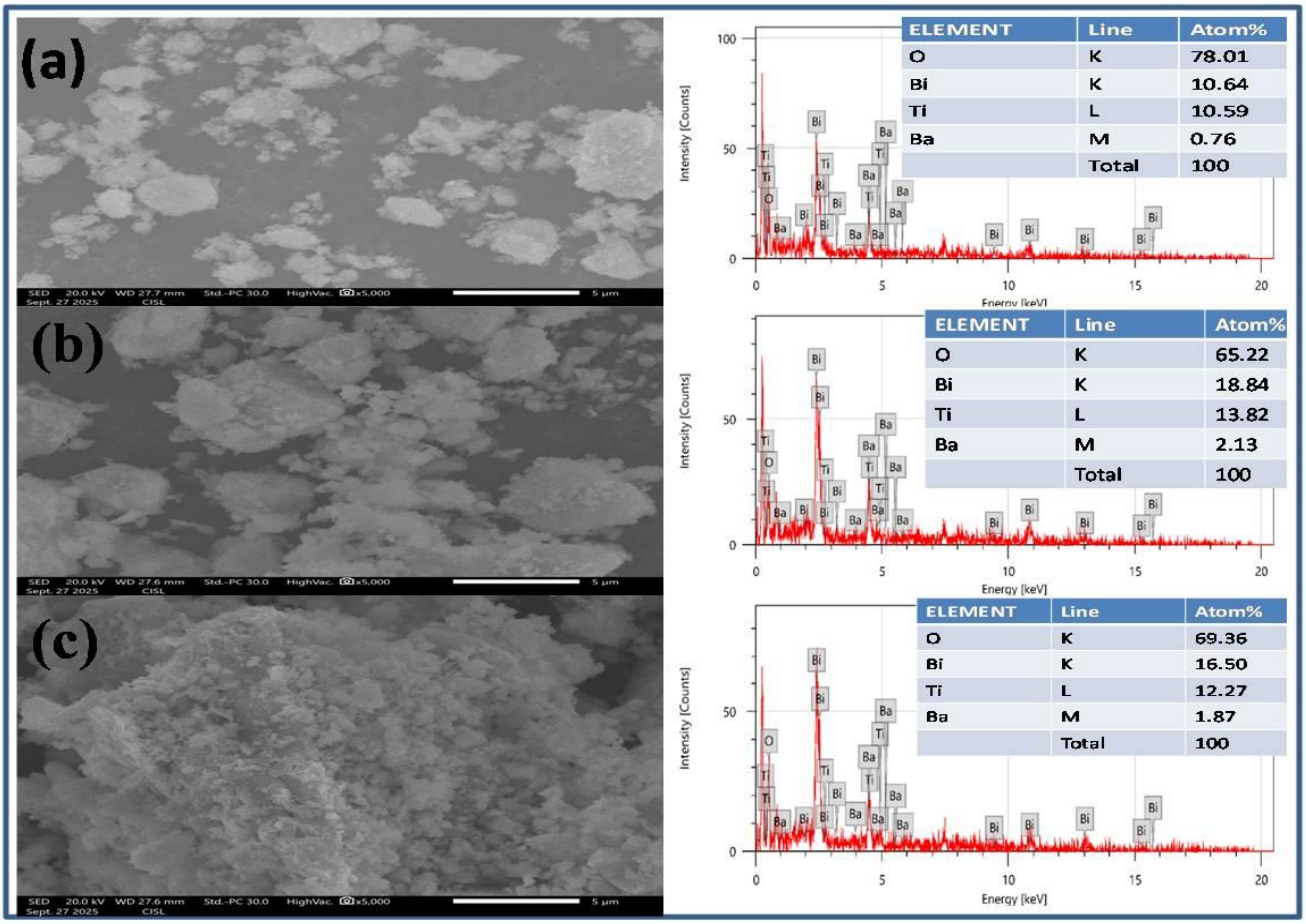

Fig. 3 SEM images and EDS spectra of BBTO NPs (a) BBTO-1,(b) BBTO-2,(c) BBTO-3

3.1.3 XPS analysis

The surface of elemental composition and chemical valence states of the synthesized material were studied by XPS as shown in Figure **4**(a). The extensive survey spectrum confirms the presence of elements Bi, Ba, Ti, O and C. The C 1s peak at 284.8 eV [**26**] results from the adventitious carbon used to calibrate the binding energy scale of the XPS data. Figure **4**(b) The high resolution Bi 4f spectrum displayed two separate peaks at 158.32 and 163.65 eV corresponding to Bi $4f_{7/2}$ and Bi $4f_{5/2}$ respectively, which confirmed the presence of Bi^{3+}[**27**]. Figure **4**(c) Ti 2p spectrum with peaks at 457.55 and 464.76 eV for Ti $2p_{3/2}$ and Ti $2p_{1/2}$, respectively, indicating Ti^{4+}[**28**]. Figure **4**(d) The O 1s core level at 529.2 eV is oxygen[**29,30**]. Figure **4**(e). The Ba 3d doublet at 779.6 and 795.0 eV assigned to Ba $3d_{5/2}$eV and $3d_{3/2}$eV [22] respectively, confirms the existence of Ba^{2+}. The binding energies of the Bi, Ti and O core levels in the XPS spectra change correspondingly with the structural changes observed by XRD, indicating that the Ba addition alters both the extended crystal structure and the the local chemical environment of constituent atoms.

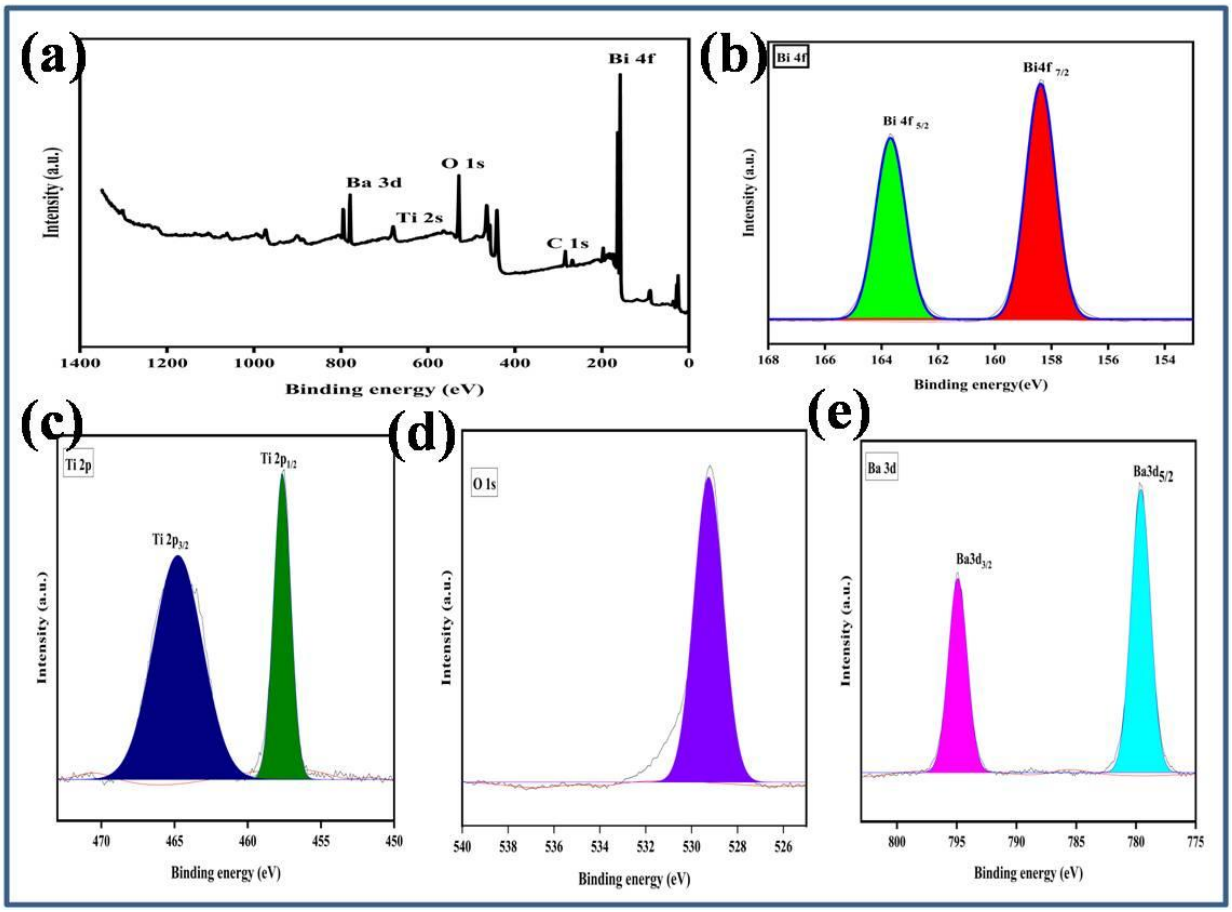

Fig. 4 (a) XPS survey spectrum and high-resolution spectra of (b) Bi 4f, (c) Ti 2p and (d) O 1s (e) Ba 3d for BBTO-2 NPs

3.1.4 UV-DRS analysis

Figure **5**(a) shows The optical characteristics and electronic bandgap energies of synthesized samples BBTO-1, BBTO-2 and BBTO-3 were analyzed by UV-DRS spectroscopy as shown in the figure. The absorption spectra show a high absorption of UV to near visible light with a main absorption edge at 400–420 nm. Direct bandgap values were obtained using Tauc's figure [21].

$$(\alpha h\upsilon)^{\frac{1}{n}} = A(h\upsilon - E_g) \qquad (8)$$

Here, hυ is the energy of the incident photon, A is a constant of proportionality and n is equal to 1/2 in the case of direct electronic transitions. The band gap energies for the synthetic materials are estimated from Tauc plots of $(\alpha h\upsilon)^2$ versus hυ. The calculated values of the (Eg) band gap indicate the influence of Ba modification on the optical response of $Bi_4Ti_3O_{12}$ .The band gap energies for BBTO-1, BBTO-2 and BBTO-3 were calculated to be around 2.78 eV, 2.75 eV and 2.82 eV respectively. Figure **5**(b) BBTO-2 lower band gap indicates the enhanced photon absorption capacity, which is beneficial for optoelectronic and photocatalytic applications [**31,32**].

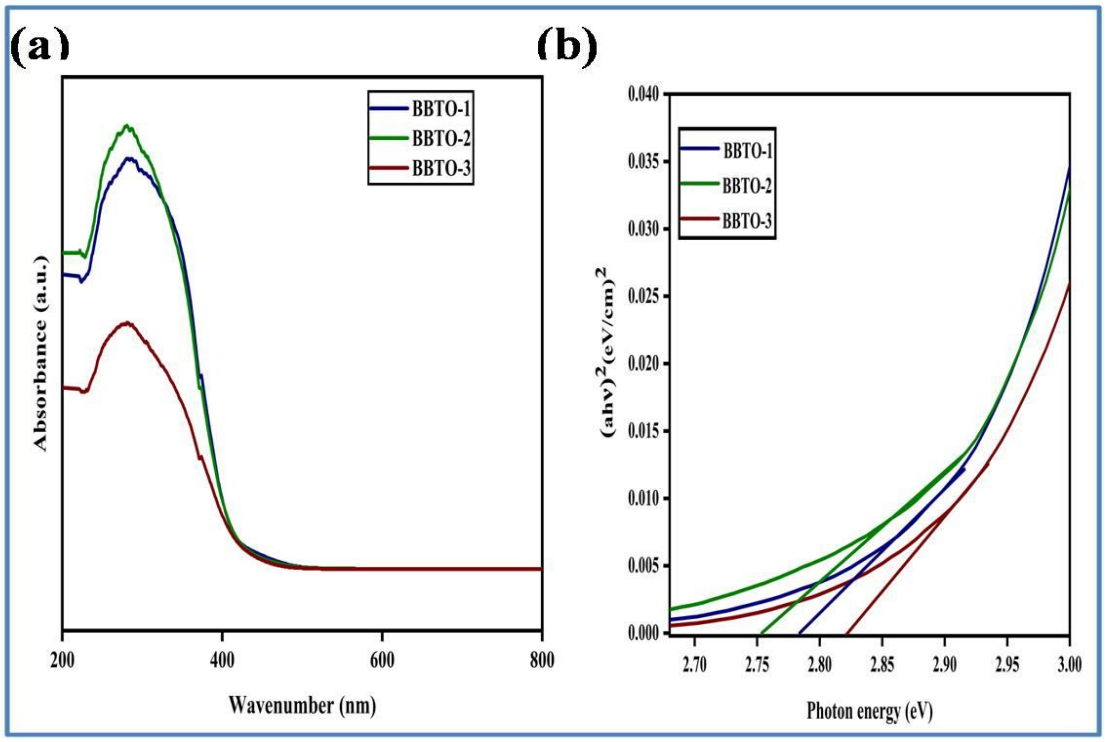

Fig 5 (a) UV–DRS spectra and (b) Tauc plots of BBTO NPs (a) BBTO-1,(b) BBTO-2,(c) BBTO-3

3.1.5 PL analysis

The PL emisson spectra are shown in Figure **6** to study the recombination behavior of the photogenerated electron-hole pairs in BBTO-1, BBTO-2 and BBTO-3 samples. The spectra demonstrate a sharp peak of the emission at 650 nm with the broad emission in the region of 400-550 nm, which is related to the intrinsic defect states and oxygen vacancies. BBTO-1, BBTO-3 showed the high PL intensity among all the samples, indicating a high rate of charge carrier recombination. Meanwhile, BBTO-2 has the lowest PL emission intensity, indicating that the photogenerated electrons and holes are well separated and the recombination is reduced. Such improved charge separation efficiency is more favorable for photocatalytic and photoelectrochemical applications [**33,34**]. The analysis of PL spectra together with UV-DRS and XPS spectra indicates that the Ba modification changes the electrical and surface defect environment of $Bi_4Ti_3O_{12}$. The efficient photocatalytic degradation performance of the optimized BBTO sample could be attributed to these modifications.

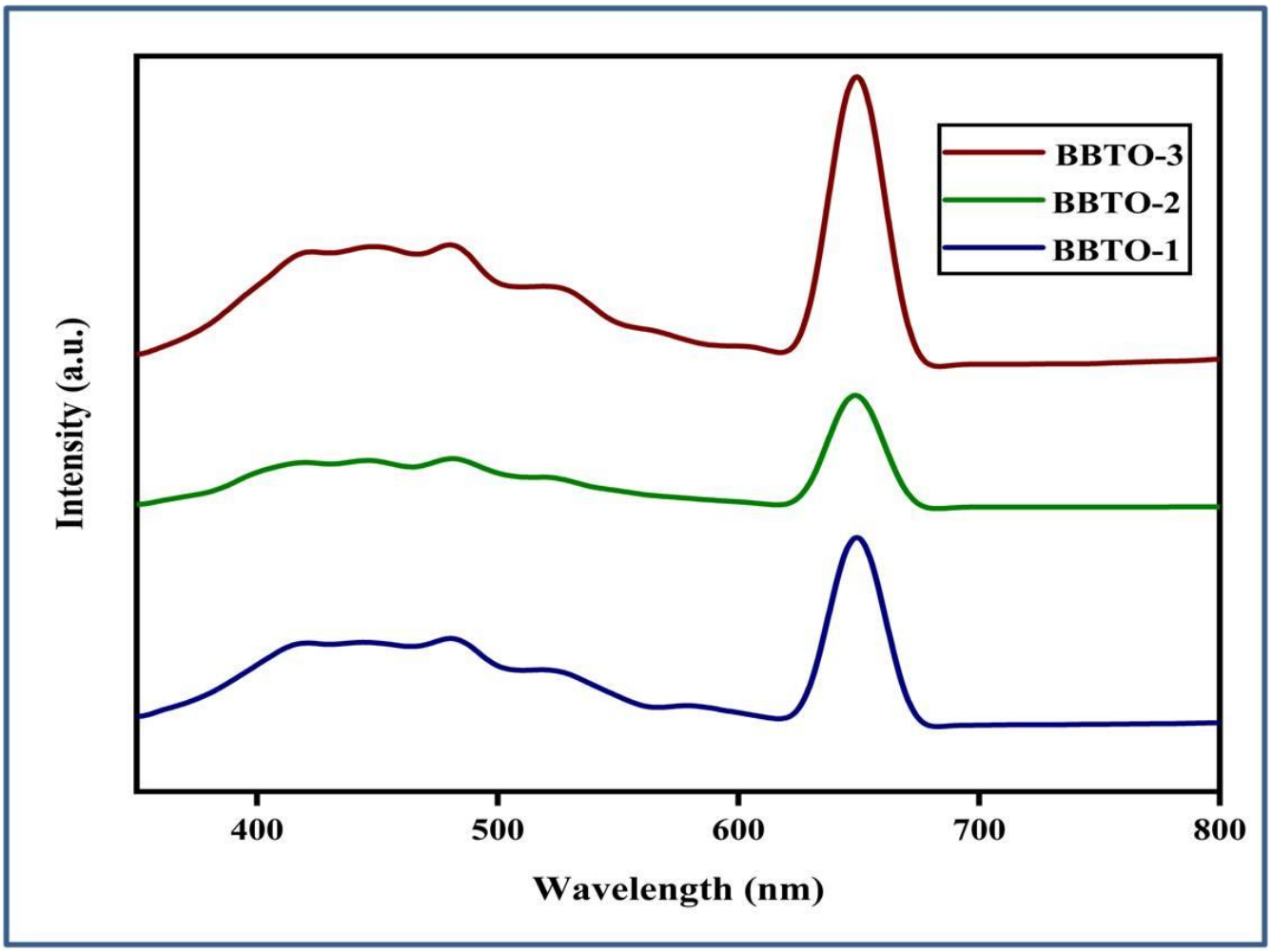

Fig. 6 PL spectra of BBTO Nps (a) BBTO-1,(b) BBTO-2,(c) BBTO-3

3.2 Electrochemical Studies

3.2.1 CV analysis

electrochemical The performance of electrochemical and charge-storage kinetics of the prepared electrode materials were assessed by CV measurements at varying scan rates (5-100 mV s^{-1}) in the potential window 0-0.45 V Figure **7**. The unique paired anodic and cathodic peaks in the CV profiles [**35**] suggest that reversible Faradaic redox processes contribute a significant part of the entirety charge-storage mechanism. The anodic and cathodic peak currents increase gradually with the scan rate, but the CV profiles usually keep the same shape. This behavior suggests favorable ion-transport kinetics within the electrode and good electrochemical reversibility [**36**]. The small change in peak position and current response at higher scan rates may be attributed to increased polarization and diffusion limitations of electrolyte ions. These results suggest that the synthesized electrode maintains its electrochemical response over the whole range of scan rates examined and has a significant pseudocapacitive behaviour. shows the effect of the scan rate on the capacitance measured by CV methods. The specific capacitance (C_s) was calculated from the CV curves and Eq (1) to be 735, 512, 393, 273, 150 and 89 Fg^{-1} at 5-100 mV/s

respectively. Clearly, the specific capacitance decreases with increasing of scan rate. Thus it was shown that the CV tends to give a higher capacitance at low scan rates and a smaller capacitance at high scan rates. It is thought that slowing down the scan rate allows more of the electrolyte to enter the pores and make contact with the inside surface of the electrode material resulting in a higher capacitance. The decrease in specific capacitance at higher scan rates can be attributed to the limited diffusion of electrolyte ions to the internal active sites of the electrode at higher scan rates. [**37**].

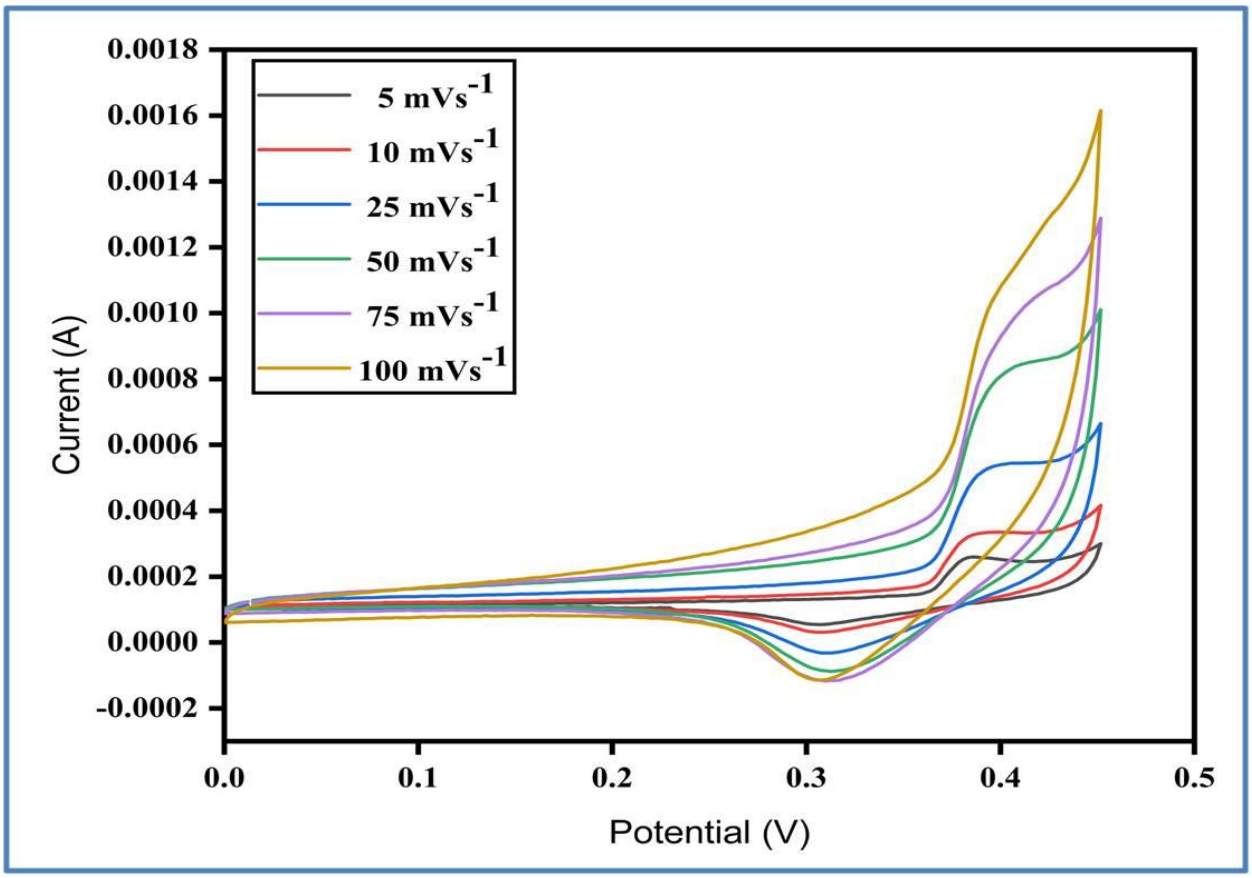

Fig. 7 CV curves of BBTO-2 at different scan rates

In order to obtain a better understanding of the charge storage mechanism, the relationship between peak current (i) and scan rate (v) was studied using the power-law equation[**38**].

$$i = av^b \qquad (9)$$

where i is the peak current and v is the scan rate. a and b are tunable constants. is calculated by taking the log of both sides.

$$\log i = \log a + \log v \qquad (10)$$

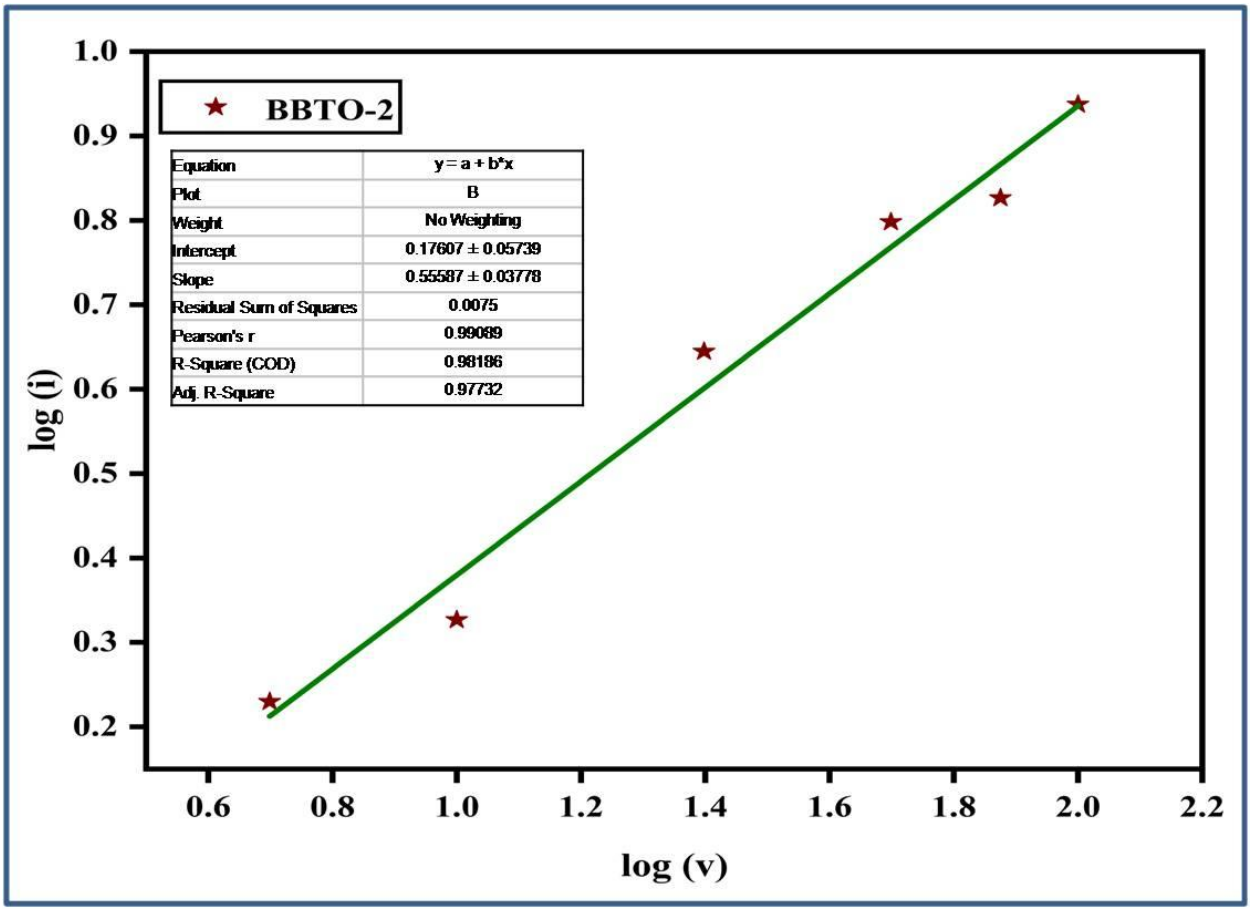

Fig. 8 Kinetic analysis of BBTO-2 electrode, b value determination

The b value was determined from the slope of the linear plot of log(i) versus log(v) as shown in Figure **8.** The calculated b-value for cathodic peaks is 0.55 with correlation coefficient (R^2) of 0.98186. The obtained b-value suggests that the charge storage mechanism of the BBTO-2 electrode is mainly dominated by diffusion-controlled Faradaic reactions, whereas the capacitive – controlled play a minor role. The excellent penetration of the electrolyte ions into the active material at reduced scan rates allows us to get the best use of the electrochemically active areas. The charge-storage behavior is dominated by surface-controlled capacitive processes and ion diffusion is more limited at higher scan rates. The results demonstrate that the electrochemical activity of the BBTO-2 electrode is influenced by the diffusion-controlled Faradaic reactions and surface-controlled capacitive processes.

3.2.2 GCD analysis

The performance electrochemical storage and specific capacitance of the synthesized electrode were evaluated by GCD experiments at different current densities in the range of 1-5 A g^{-1} Figure **9**. The GCD profiles show non-linear and quasi-symmetrical charge-discharge features confirming the pseudocapacitive nature of the electrode and the contribution of reversible Faradaic reactions in the total charge storage process[**39**]. The specific

capacitance (C_s) of 1-5 A g^{-1} was calculated from the GCD curves by using Eq (2), 691 Fg^{-1}, 355 Fg^{-1}, 272 Fg^{-1}, 154 Fg^{-1} and 88 Fg^{-1}. The long discharge time at low current density of 1 Ag^{-1} is due to the sufficient interaction between the electrolyte ions and the electrochemically active sites, which results in the high specific capacitance. The specific capacitance decreased gradually with the increase of current density because of the decrease of discharge time [**40,41**]. This behavior is caused by the limited diffusion and lower utilization of active sites at higher current densities. The initial part of the discharge curves is characterized by a small IR drop[**42**], indicating that the electrode exhibits high charge-transfer properties and relatively low internal resistance. Thus, the GCD results demonstrate that the electrode has an acceptable rate capability and a good pseudocapacitive charge storage behavior.

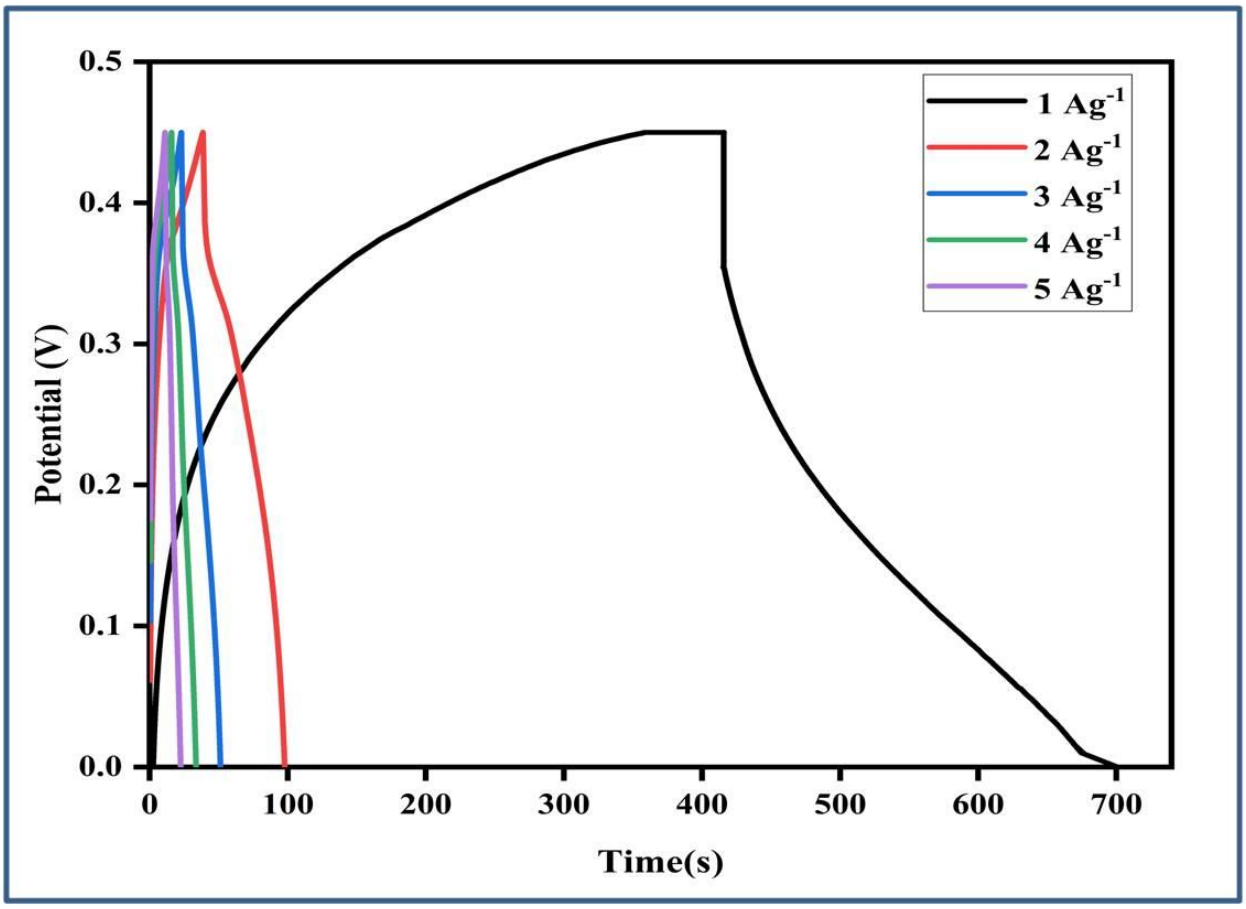

Fig. 9 GCD curves of BBTO electrodes at different current densities

3.2.3 EIS analysis

The internal resistance of the electrode material, charge transfer kinetics and ion transport characteristics were analyzed by EIS. Figure **10**(a)The inset shows the fitted Nyquist plot and the corresponding Randles-type equivalent circuit (Rs(Rp‖CPE)). The low value of the solution resistance (Rs = 1.48 Ω) indicates a good electrical contact and low ohmic resistance of the electrode/electrolyte system. To account for the surface heterogeneity and non-ideal capacitive response, a constant phase element (CPE) was added with Y0 = 1.49 mMho.s^N and N = 0.744.

The charge transfer resistance (Rp) was modeled as (Rp=7.44 kΩ). The linear trend observed at lower frequencies also indicates efficient kinetics of ion diffusion during electrochemical operations[**22,43,44].** Therefore, the EIS data provides more evidence for the role of Ba alteration on the interfacial charge transfer and ion transport properties of $Bi_4Ti_3O_{12}$. The frequency dependent impedance behavior of the synthesized electrode from 1 to 100,000 Hz was further analyzed via Figure **10**(b)Bode plots. The phase angle 70° and the impedance magnitude is relatively high at low frequencies, which indicates predominantly capacitive behavior and effective charge accumulation at the electrode–electrolyte interface. The impedance magnitude decreases with increasing frequency and the phase angle also decreases. This behavior shows a transition from a low-frequency capacitive response to a more resistive response at higher frequencies. At high frequencies, the phase angle tends to approach nearly 0°, indicating that the impedance response is dominated by the ohmic resistance of the electrode/electrolyte system. The frequency-dependent transition reveals the charge-storage and transport processes taking place in the electrode, while the large phase angle observed in the low-frequency region indicates the favorable capacitive nature of the electrode[**45**].

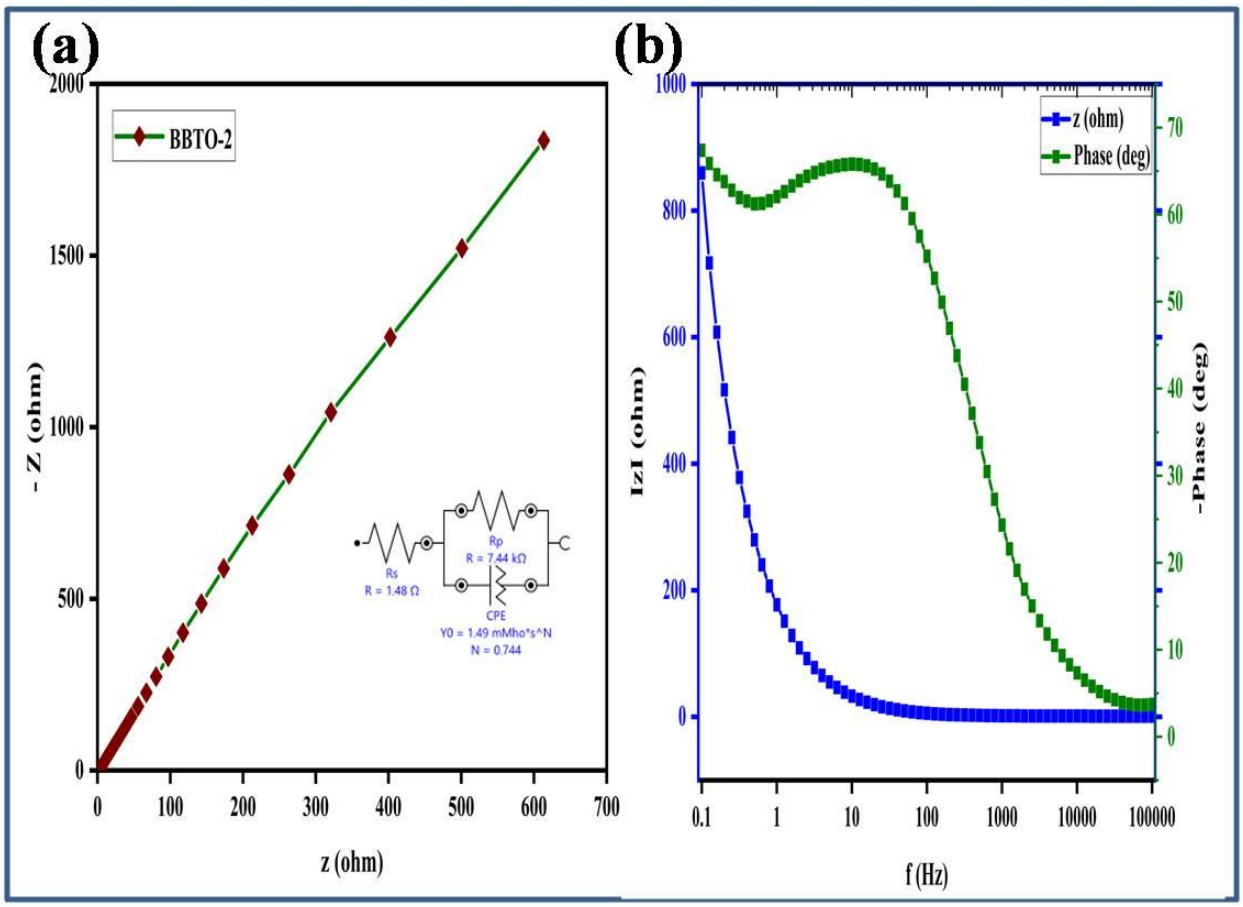

Fig. 10 (a) Nyquist plots (b) Bode plots of BBTO-2 electrode

The general energy storage capacity **Fig. 11** was determined by plotting a Ragone plot to show the correlation between energy density and power density. The assembled supercapacitor device showed the highest energy density of 18.87 Wh kg^{-1} at the power density of 225 W kg^{-1}. The electrode still had an energy density of 2.5

Wh^{-1} at a high power density of 1123 W kg^{-1}. This energy-power density demonstrates the promise of the synthesized material for energy storage applications[**46**].

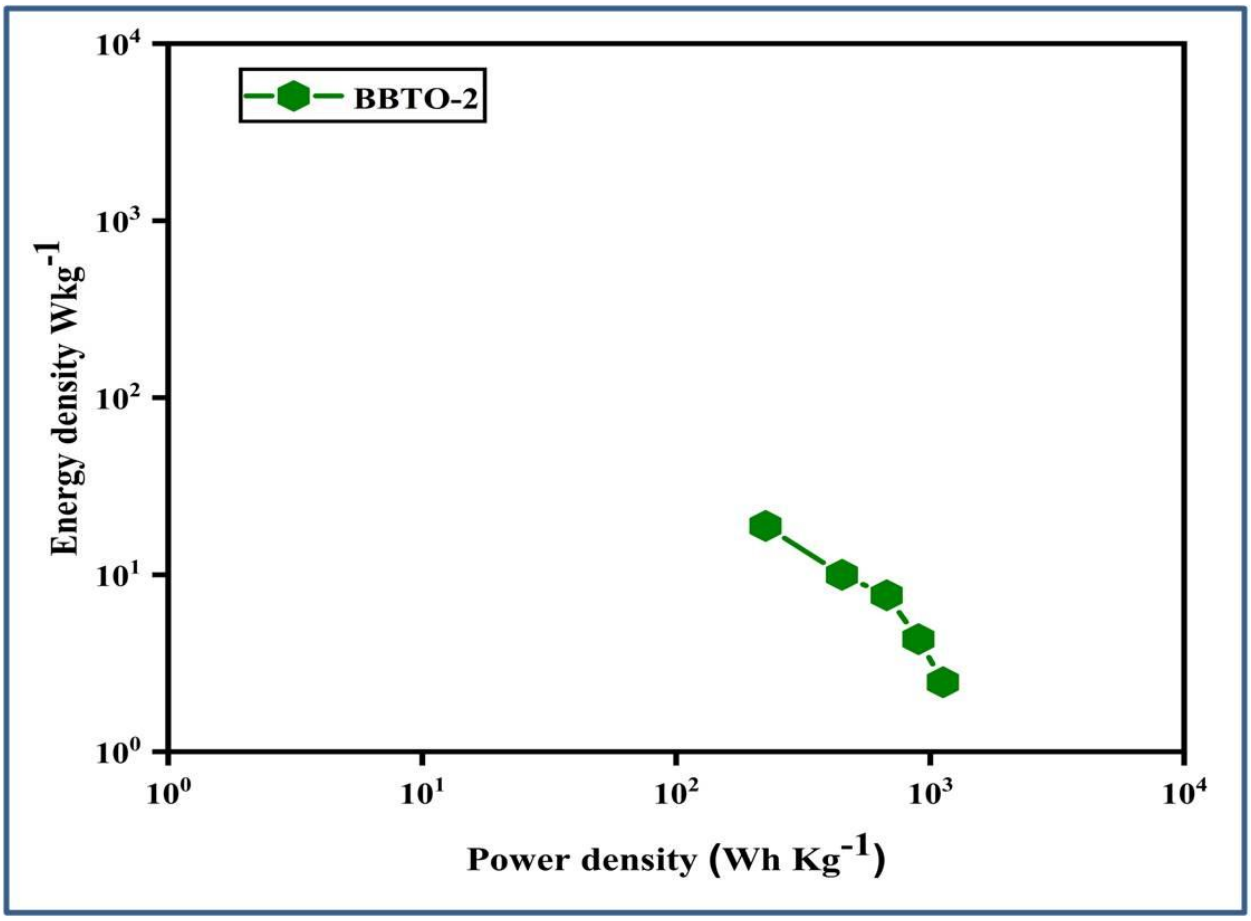

Fig. 11 Ragone plot of the BBTO-2 electrode

3.2.4 Stability

The long-term cycling stability is an important consideration for the practical durability of energy storage materials. The electrochemical stability and Coulombic efficiency of the electrode were evaluated over 2000 continuous charge-discharge cycles as shown in the Figure **12.** The material initially has 100 % efficiency that decreases slowly in long-term cycling. The electrode still retains a high Coulombic efficiency of 82% over 2000 cycles. This performance shows good structural stability and reversible charge transfer ability during the repeated charge-discharge processes [**21**].

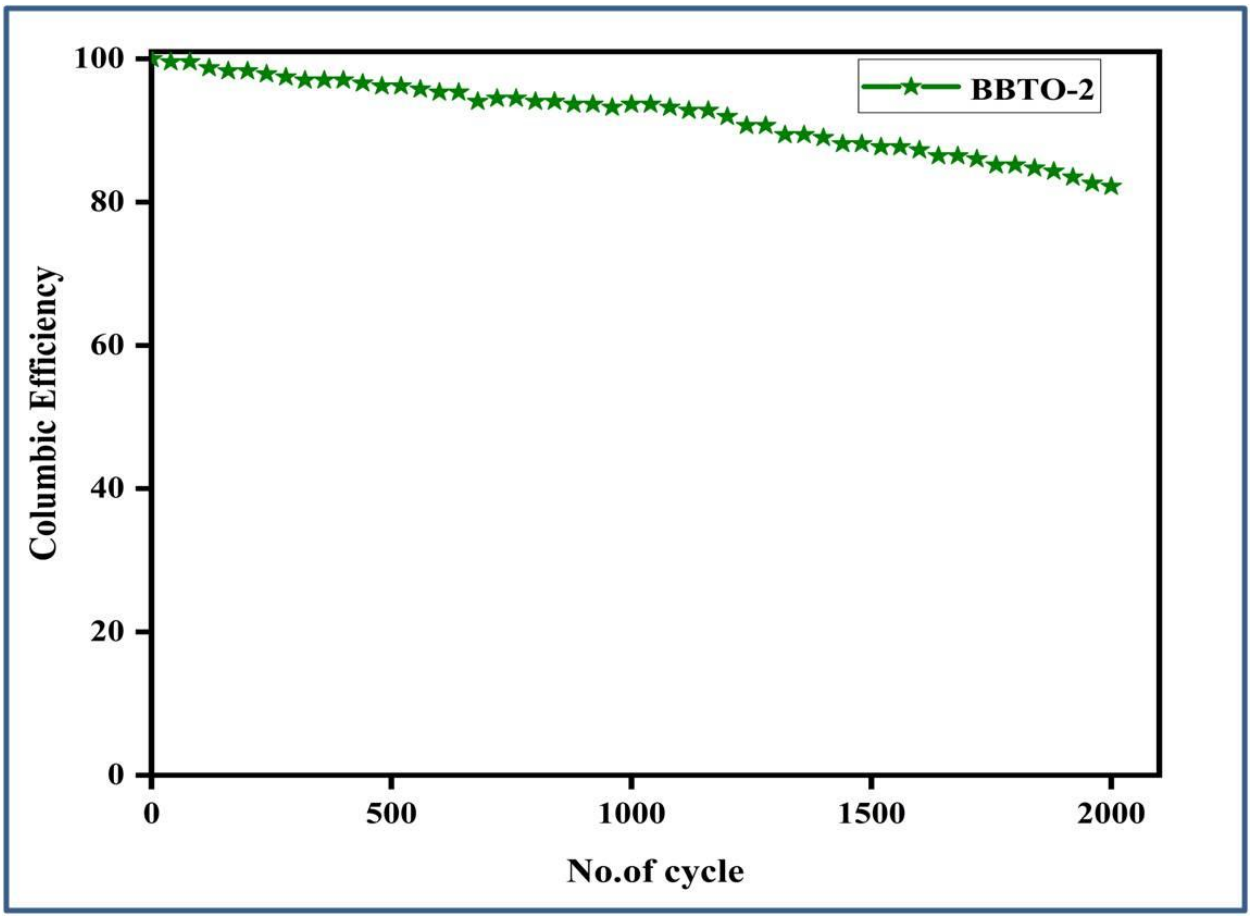

Fig. 12 Cycling stability and coulombic efficiency of the BBTO-2 electrode

Table. 1
Comparing our research with previously published composites in three electrode configurations

Sample	Electrolyte	Synthesis method	Specific Capacitance F/g	Current density A/g	Ref
Sr_2CoO_5@ 15%rGO	2 M KOH	Solvothermal	230.95	0.6	[**47**]
rGO/$NiFe_2O$	1M Na_2SO_4	Microwave	210.9	0.5	[**48**]

$_4$		absorbtion			
La_2CuMnO_6	2M KOH	First-principle method	205.5	0.5	[**49**]
UU 200/Bi_4O_8	1 M KOH	Solvothermal	220	1	[**50**]
ZIF_8/ZIF_{67}/ MWCNT	2 M KOH	Self assembly	194.48	0.8	[**51**]
CNT@CZIF -2	6 M KOH	Polydopamine coating	324	0.5	[**52**]
$Bi_4Ti_3O_{12}$ (BTO-1)	1 M KOH	Co-precipitation	595	1	[**53**]
BBTO-2	1MKOH	Co-precipitation	691	1	This work

3.3 Photo catalytic

The catalytic degradation efficiency of the synthesized catalyst was evaluated by monitoring the UV-Vis absorption spectra of the organic dye MB solution as a function of time under light irradiation at regular time intervals (0-80 min). The Figure **13** shows that the initial dye solution (0 min) has a characteristic maximum absorption peak at 664 nm. The intensity of the absorption peak was observed to decrease continuously and significantly with time upon exposure to the catalyst and light irradiation [**21,54**]. After 80 min of reaction, the main absorption peak nearly disappears completely, confirming the almost complete decolorization and high catalytic degradation efficiency toward the target organic pollutant.

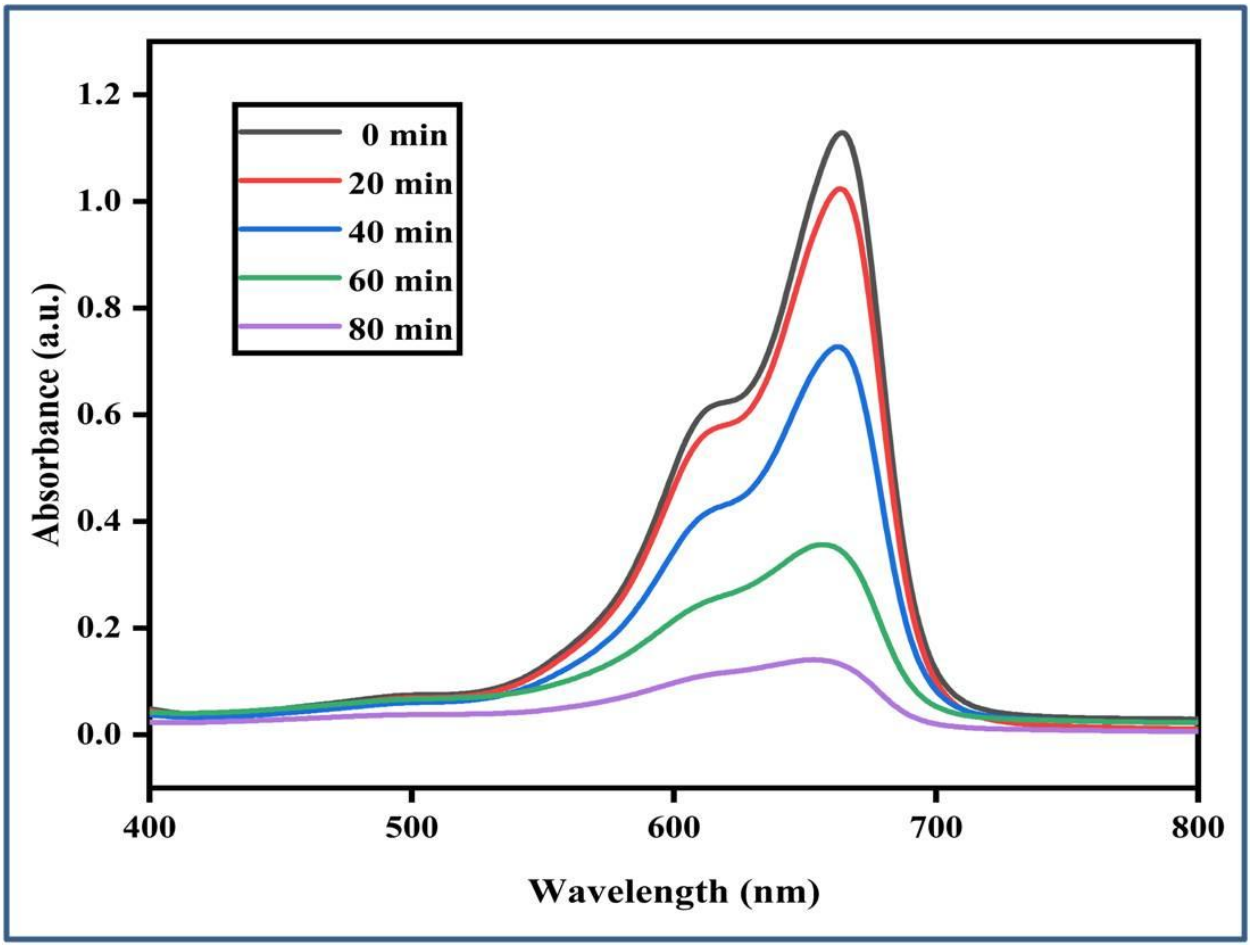

Fig. 13 UV–Visible absorption spectra of MB degraded using BBTO-2 under sunlight irradiation.

The degradation efficiency of the BBTO-2 sample was calculated at regular time intervals as shown in the Figure **14**(a) . It starts from zero at the initial exposure of 0%, then the degradation efficiency rapidly increases to about 12% at 20, 35% at 40 and reaches to 68% at 60. BBTO-2 reaches the maximum degradation efficiency of 87% in 80 of the total reaction time. The rate of degradation is very fast which demonstrates the high catalytic efficiency and better charge-transfer reactivity of BBTO-2 sample toward the removal of pollutant.

The photocatalytic activity of the sample BBTO was evaluated by the normalized concentration ratio (C/C_0) of dye pollutant versus irradiation time as shown in the Figure **14**(b). The concentration of the target molecule decreases constantly with light exposure at before irradiation . The ratio decreased to 0.14 after of continuous irradiation, indicating that 87% of the initial pollutant was degraded. This rapid decay also further supports the efficient photoreactivity and strong degradation capability of the BBTO-2 catalyst.

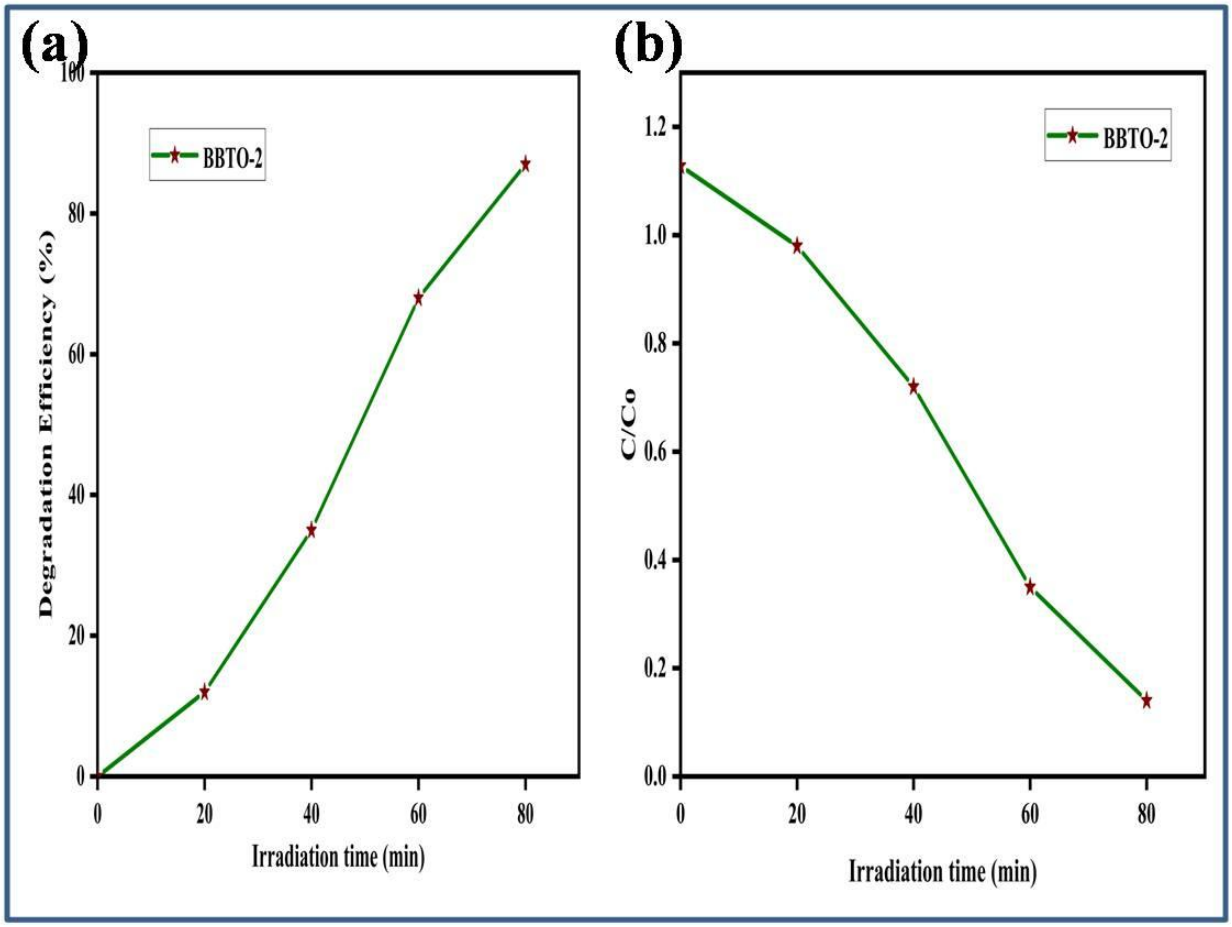

Fig. 14 (a) Photocatalytic degradation efficiency and (b) normalized concentration (C/C_0) of MB for BBTO-2 NPs under sunlight irradiation.

Table 2
Shows a comparison of our results with previous studies on photocatalysis

Sample	Method	Dye	Light	Reactant Solution	Degradation (%)	min	Ref
TaON	Deposition precipitation method	MB	300 W Xe lamp	100 mL	88	120	**[55]**
WO_3	Hand milling method	CH_3CHO	150 W Xe lamp	0.5 L air	51	240	**[56]**
TiO_2	Liquid phase depositionmethod	MB	20 W low-pressure mercury lamp	60 mL	72	240	**[57]**

H_2WO_4 .H_2O	One step ionic reaction	MO	55 W fluorescence lamp	10 mL	87	240	**[58]**
Ba/Fe $Bi_4Ti_3O_{12}$	Molten salt method	Rh-B	Sunlight	100mL	96	180	[**59**]
BBTO-2	Co-precipitation method	MB	Sunlight	150mL	87	80	This work

Conclusion

In this study, Ba-Modified $Bi_4Ti_3O_{12}$ nanoparticles were synthesized, and controlled Ba doping achieved great improvements in electrical energy storage and photocatalytic activity. The XRD, XPS and EDX analyzes confirmed phase purity and substitution induced structural modifications without disturbing the parent crystal structure. Out of all the compositions, the optimized BBTO-2 sample exhibited the performance with a specific capacitance of 691 Fg^{-1} at $1Ag^{-1}$ and Degradation 87% degradation of MB dye under sunlight within 80 min. These enhancements are directly attributed to the improved charge-carrier separation kinetics and the reduced interfacial charge-transfer resistance. Modification of Ba provides an effective pathway to obtain multifunctional bismuth titanate materials for energy storage and environmental application.

Funding Information

The authors received no specific funding for this wok.

Conflict Of Interest

The authors declare that they have no competing interest.

Acknowledgement

The corresponding author expresses gratitude to the Centralized Instrumentation and Service Laboratory (CISL) and the Department of Physics at Annamalai University in Annamalai Nagar, Tamil Nadu, India, for granting access to DST-FIST-supported instrumental and analytical facilities that were crucial to this study.

Author contributions

S. Sneka contributed to writing−original draft, methodology, formal analysis, data curation, & conceptualization. Dr. V. Ananthi writing - review editing, supervision, methodology, investigation, & formal analysis. Dr. G. Sivakumar contributed electrochemical measurements to writing - review editing, supervision, methodology, investigation, & formal analysis and Dr. S. Ramanathan supervision, review and editing.

Reference

1. Libich J, Maca J, Vondrak J, Cech O, Sedlarikova M (2018) Supercapacitors: Properties and applications. Journal of Energy Storage 17:224–227. https://doi.org/10.1016/j.est.2018.03.012
2. Pershaanaa M, Bashir S, Ramesh S, Ramesh K (2022) Every bite of Supercap: A brief review on construction and enhancement of supercapacitor. Journal of Energy Storage 50:104599. https://doi.org/10.1016/j.est.2022.104599
3. Gopi C.V.V.M, Alzahmi S, Narayanaswamy V, Vinodh R, Issa B, Obaidat I.M (2025) Supercapacitors: A promising solution for sustainable energy storage and diverse applications. Journal of Energy Storage 114 115729. https://doi.org/10.1016/j.est.2025.115729
4. Ahuja R, Srivastava R (2024) Introduction to Photocatalytic Materials for Clean Energy, Renewable Chemicals production, and Sustainable Catalysis. Nanoscale Adv., 6:3695–3698. DOI: 10.1039/d4na90075h

5. Wang L, Li H, Zhang S, Long Y, Li L, Zheng Z, Wu S, Zhou L, Hei Y, Luo L, Jiang F (2019) One-step synthesis of $Bi_4Ti_3O_{12}/Bi_2O_3/Bi_{12}TiO_{20}$ spherical ternary heterojunctions with enhanced photocatalytic properties via sol-gel method. Solidstatesciences 2019:106098. https://doi.org/10.1016/j
6. Varshney G, Kanel S.R, Kempisty D.M, Varshney V, Agrawal A, SahleDemessie E, Varma R.S, Nadagouda M.N (2016) Nanoscale TiO_2 films and their application in remediation of organic pollutants. Coord. Chem. Rev. 306:43–64. DOI:10.1016/j.ccr.2015.06.011
7. Yao W.F, Wang H, Xu X.H, Zhou J.T, Yang X.N, Zhang Y, Shang S.X, Wang M (2003) Sillenites materials as novel photocatalysts for methyl orange decomposition, Chem. Phys. Lett. 377:501–506. DOI:10.1016/S0009-2614(03)01209-0
8. Tian J, Sang Y, Yu G, Jiang H, Mu X, Liu H (2013) A Bi_2WO_6-based hybrid photocatalyst with broad spectrum photocatalytic properties under UV, visible, and near-infrared irradiation. Adv. Mater. 25: 5. https://doi.org/10.1002/adma.201302014
9. Lv H, Liu Y, Rehman A.U., Kan K, Zhang W, He L, Wang Y, Wang R, Shi K (2019) Intercalation of Bi_2O_3/Bi_2S_3 nanoparticles into highly expanded MoS_2 nanosheets for greatly enhanced gas sensing performance at room temperature. J. Hazard Mater. 363:335–345. https://doi.org/10.1016/j.jhazmat.2018.09.077
10. Su W.N, Ayele D.W, Ochie V, Pan C.J, Hwang B.J (2014) The development of highly crystalline single-phase $Bi_{20}TiO_{32}$ nanoparticles for light driven oxygen evolution. Applied Catalysis B: Environmental 150-151 363– 369. http://dx.doi.org/10.1016/j.apcatb.2013.12.033
11. Navarro-Rojero M.G, Romero J.J, Rubio-Marcos F, Fernandez J.F (2010) Intermediate phases formation during the synthesis of $Bi_4Ti_3O_{12}$ by solid state reaction. Ceramics International 36:1319–1325. doi:10.1016/j.ceramint.2009.12.023
12. Stojanovic B.D, Simoes A.Z, Paiva-Santos C.O, Quinelato C, ongo E.L, Varela J.A (2006) Effect of processing route on the phase formation and properties of $Bi_4Ti_3O_{12}$ ceramics. Ceramics International 32 :707–712. doi:10.1016/j.ceramint.2005.05.007
13. Concha-Balderrama A, Martinez-Rodriguez H.A., Rojas-George G, EsparzaPonce H.E, Orozco-Carmona V, Piza-Ruiz P, Bocanegra-Bernal M.H, Reyes-Rojas A (2018) Enhanced ionic transport and compressive residual stress in Er-doped Bi_2O_3 with lower Er3þ concentrations, J. Electron. Mater. 47:5422–54. https://doi.org/10.1007/s11664-018-6441-0
14. Shang F, Chen S, Liang J, Liu C (2019) Preparation and photocatalytic properties of ZnO deposited TiO_2 nanotube Arrays by anodization. J. Nanosci. Nanotechnol. 19:2070–207. DOI: https://doi.org/10.1166/jnn.2019.15797
15. Lu Y, Huang Y, Zhang Y, Cao J.J, Li H, Bian C, Lee S.C (2018) Oxygen vacancy engineering of $Bi_2O_3/Bi_2O_2CO_3$ heterojunctions: implications of the interfacial charge transfer, NO adsorption and removal. Appl. Catal. B Environ. 231:357–367, https://www.sciencedirect.com/science/article/pii/S0926337318300158
16. Medina J.C, Portillo-Velez N.S, Bizarro M, Hernandez-Gordillo A, Rodil S.E.(2018) Synergistic effect of supported ZnO/Bi_2O_3 heterojunctions for photocatalysis under visible light. Dyes Pigments 153:106–116. https://doi.org/10.1016/j.dyepig.2018.02.006
17. Polat Y, Arı M, DagdemirY (2018) Magnetic Properties of Co-doped Bismuth Oxide (δ-Bi_2O_3) at Low Temperature. Journal of Low Temperature Physics 193:74–84. https://doi.org/10.1007/s10909-018-2046-5
18. Hernandez-Gordillo A, Vazquez L, Ramos J, Bizarro M, Rodil S.E (2018) The role of the molar ratio of (HNO_3/Bi_3þ) on the formation and morphology of alpha-Bi_2O_3 microrods with photocatalytic properties. Mat. Sci. Semicon. Proc. 86:93–100. https://doi.org/10.1016/j.mssp.2018.06.024
19. Kim M.W, Samuel E, Kim K, Yoon H, Joshi B, Swihart M.T, Yoon S.S (2018) Tuning the morphology of electrosprayed $BiVO_4$ from nanopillars to nanoferns via pH control for solar water splitting. J. Alloys Compd. 769:193–200. https://doi.org/10.1016/j.jallcom.2018.07.167

20. Suhaimy S.H.M, Lai C.W, Tajuddin H.A, Samsudin E.M, Johan M.R (2018) Impact of TiO_2 nanotubes morphology on the photocatalytic degradation of simazine pollutant. Materials 11.11:2066. https://doi.org/10.3390/ma11112066
21. Selvakumar P, Thiyagarajan S, Ganesan S, Calisius S (2025) Multifunctional nickel tungstate nanoparticles: a dual approach for high-performance supercapacitors and antimicrobial applications. Eur. Phys. J. Plus 140:651. https://doi.org/10.1140/epjp/s13360-025-06590-9
22. Sarathkumar A, Nithishkumar S, Sivakumar G, Mohanraj K (2025) Innovative electrochemical performance of Cu_2BaSnS_4 and its photocatalytic activity. Materials Science in Semiconductor Processing 196:109660. https://doi.org/10.1016/j.mssp.2025.109660
23. Subohi O, Bowen C.R, Malik M.M, Kurchania R (2016) Dielectric spectroscopy and ferroelectric properties of magnesium modified bismuth titanate ceramics, Journal of Alloys and Compounds 688:27e36. DOI:10.1016/j.jallcom.2016.07.173
24. Abdel-Kader S.R, El-Awad A.M, Abdel Rahim M.A (2026) Influence of calcination temperature on the properties and photocatalytic efficiencies of $BiFe_{0.9}Cu_{0.1}O_3$ nanoparticles. Scientific Reports 16:4387. https:// doi.org/10.1038/s41598-025-34901-8.
25. Cui M, Kang L, Shi M, Xie L, Wang X, Zhao Z, Yun S, Liang W (2017) Explore the influence of agglomeration on electrochemical performance of an amorphous MnO_2/C composite by controlling drying process. Applied Surface Science 416:241-247. https://www.sciencedirect.com/science/article/pii/S0169433217311674
26. X. Zhao, H. Yang, S. Li, Z. Cui, C. Zhang, Synthesis and theoretical study of large-sized $Bi_4Ti_3O_{12}$ square nanosheets with high photocatalytic activity. Materials Research Bulletin 107 (2018) 180-188, https://doi.org/10.1016/j.materresbull.2018.07.018.
27. Zhao X, Yang H, Cui Z, Li R, Feng W (2017) Enhanced photocatalytic performance of Ag–$Bi_4Ti_3O_{12}$ nanocomposites prepared by a photocatalytic reduction method. Materials technology 32.14:870-888. https://doi.org/10.1080/10667857.2017.1371914.
28. Li N, Wu J, Fang H.B, Zhang X.H, Zheng Y.Z, Tao X (2018) Au-nanorod-anchored {0 0 1} facets of $Bi_4Ti_3O_{12}$ nanosheets for enhanced visible-light-driven photocatalysis, Applied Surface Science 448 41-49. https://doi.org/10.1016/j.apsusc.2018.04.066
29. Liu J, Sun M, Chang M.J, Cui W.N, Zhang C.M, Ni F.R, Zhang J, Fan S.M, Du H.L (2021) Novel TiO_2/$Bi_4Ti_3O_{12}$ nanorod arrays decorated with Co-Pi for boosted solar photoelectrochemical water splitting. Journal of Physics and Chemistry of Solids 157:110179. https://doi.org /10.1016/j.jpcs.2021.110179
30. Wang L, Ma W, Fang Y, Zhang Y, Jia M, Li R, Huang Y (2013) $Bi_4Ti_3O_{12}$ synthesized by high temperature solid phase method and it's visible catalytic activity. Procedia Environmental Sciences 18:547-558. doi: 10.1016/j.proenv.2013.04.074
31. Bansal H, Sethi P, Basu S, (2025) Nanoflower-like ZnO–carbon quantum dot heterostructures for solar-driven degradation of methylene blue: A high-performance and recyclable photocatalyst for sustainable wastewater treatment. Materials Advances 6.20:7585-7598. DOI: 10.1039/d5ma00804b.
32. Guo Y, Li J, Gao Z, Zhu X, Liu Y, Wei Z, Zhao W, Sun C (2016) A simple and effective method for fabricating novel p–n heterojunction photocatalyst g-C_3N_4/$Bi_4Ti_3O_{12}$ and its photocatalytic performances. Applied Catalysis B: Environmental 192:57-71. DOI: 10.1016/j.apcatb.2016.03.054
33. H. Shi, J. Fu, W. Jiang, Y. Wang, B. Liu, J. Liu, H. Ji, W. Wang, Z. Chen, Construction of g-C_3N_4/$Bi_4Ti_3O_{12}$ hollow nanofibers with highly efficient visible-light-driven photocatalytic performance, Colloids and Surfaces A: Physicochemical and Engineering Aspects 615(2021) 12606,DOI: 10.1016/j.colsurfa.2020.126063.
34. Gu H, Hu Z, Hu Y, Yuan Y, You J, Zou W (2008) The structure and photoluminescence of $Bi_4Ti_3O_{12}$ nanoplates synthesized by hydrothermal method. Colloids and Surfaces A: Physicochemical and Engineering Aspects 315.1-3:294-298. DOI: 10.1016/j.colsurfa.2007.08.010

35. Boudene I, Oubakalla M, Bouji M.El, Belakhmima R.A, Beraich M, Zarrouk A, Touhami M.E (2025) Superior energy storage performance of metastable β-Bi2O3 nanostructured electrode for advanced supercapacitor applications, Journal of Energy Storage 136:118519. DOI: 10.1016/j.est.2025.118519.
36. Alshammari D.A, Ikram M, Baqais A, Niazi S.U.K, Irshad A, Amin M.A, Sohail M, Warsi M.F (2024) Synthesis and supercapacitor application studies of aluminum-lanthanum co-Doped bismuth oxide composite with N-doped reduced graphene oxide. Materials Science and Engineering: B 310:117720. DOI: 10.1016/j.mseb.2024.117720
37. Lu M, Li X, Xu X, Wang X, Zhang W (2025) In situ oxidation coating of copper bismuth oxide with polypyrrole to construct rice-like core-shell structures: Revealing prospects for high-performance asymmetric supercapacitor anodes, Journal of Colloid and Interface Science 693:137598. https://doi.org/10.1016/j.jcis.2025.137598
38. Rafique A, Naeem U, Marques A, Ferreira I, Rizwan S, Baptista A.C (2025) Understanding the capacitive and diffusion-controlled behavior of electrophoretically deposited V_2CT_x on carbon yarn as a potential anode for asymmetric devices. ACS omega 10.8 7621-7634. doi: 10.1021/acsomega.4c06035
39. Thali B.G, Agrahari D.S, Kamble R.M (2025) Harnessing the synergistic effects of fabricated novel NBO/PANI nanocomposite for asymmetric supercapacitor with remarkable electrochemical performance, Materials Today Communications 44:111854. https://doi.org/10.1016/j.mtcomm.2025.111854
40. William J.J, Babu I.M, Muralidharan G (2021) Nickel bismuth oxide as negative electrode for battery-type asymmetric supercapacitor. Chemical Engineering Journal 422:130058. DOI: 10.1016/j.cej.2021.130058
41. Nakate U.T, Patil P,. Nakate Y.T, Na S.I, Yu Y.T, Hahn Y.B (2021) Ultrathin ternary metal oxide Bi_2MoO_6 nanosheets for high performance asymmetric supercapacitor and gas sensor applications, Applied Surface Science 551 149422. DOI: 10.1016/j.apsusc.2021.149422
42. Nakate Y.T, Nakate U.T, Sangle S.S, Jadhav C, Rao B.V.B, Pandit B, Yewale M.A, Kadam S.L, Ingole R.S, Khollam Y.B (2023) Preparation, characterizations of bismuth nickel oxide nanostructured active electrode and electrochemical investigation for the energy storage application, Surfaces and Interfaces 40:103142. DOI: 10.1016/j.surfin.2023.103142
43. Aqeel M. Al (2025) Liquid-free simple synthesis of nickel cobaltite nanostructures for high-performance supercapacitors and electrocatalyst applications, Journal of Solid State Electrochemistry 29:5225-5232. https://doi.org/10.1007/s10008-025-06367-1
44. Ahirrao D.J, Wilson H.M, Jha N (2019) TiO2-nanoflowers as flexible electrode for high performance supercapacitor. Applied Surface Science 491:765-778. https://doi.org/10.1016/j.apsusc.2019.05.076
45. Galal A, Hassan H.K, Jacob T, Atta N.F (2018) Enhancing the specific capacitance of SrRuO3 and reduced graphene oxide in $NaNO_3$, H_3PO_4 and KOH electrolytes. Electrochimica Acta 260:738-747. https://doi.org/10.1016/j.electacta.2017.12.026
46. Soam A, Kumar R, Singh M, Thatoi D, Dusane R.O (2020) Development of paper-based flexible supercapacitor: bismuth ferrite/graphene nanocomposite as an active electrode material Journal of Alloys and Compounds 813:152145. https://doi.org/10.1016/j.jallcom.2019.152145
47. Shahid M, Mustafa G.M, Quader A, Ramay S.M, Shar M.A, Atiq S (2024) Reduced graphene oxide/$Sr_2Co_2O_5$ composites as electrode material for supercapacitors Diamond and Related Materials 142:110777. https://doi.org/10.1016/j.diamond.2023.110777
48. Zhang Y, Wang X, Cao M (2018) Confinedly implanted $NiFe_2O_4$-rGO: Cluster tailoring and highly tunable electromagnetic properties for selective-frequency microwave absorption Nano Research 11.3:1426-1436. https://doi.org/10.1007/s12274-017-1758-1
49. Mir S.A, Gupta D.C (2019) Understanding the origin of half-metallicity and thermophysical properties of ductile La_2CuMnO_6 double perovskite, International Journal of Energy Research 43.9:4783-4796. https://doi.org/10.1002/er.4620

50. Sarmila S, Vadivel S, Sujita P, Gopal V (2025) Harnessing the potential of UU 200/Bi_4O_8 nanocomposite to optimize energy efficiency in supercapacitor and electrocatalysis application. Applied Organometallic Chemistry 39.1e70001.https://doi.org/10.1002/aoc.70001
51. Munir O, Saleem M, Manzoor M.Z, Shahzad A, Shahid S, Arif S.M.B, Akhtar M.N (2025) Novel ZIF-8/ZIF-67 and multi-wall carbon nanotubes ternary composite: A promising electrode material for high capacitance supercapacitors Materials. Chemistry and Physics 338:30672. https://doi.org/10.1016/j.matchemphys.2025.130672
52. Wan L, Shamsaei E, Easton C.D, Yu D, Liang Y, Chen X, Abbasi Z, Akbari A, Zhang X (2017) ZIF-8 derived nitrogen-doped porous carbon/carbon nanotube composite for high-performance supercapacitor. Carbon N. Y. 121:330-336. DOI: 10.1016/j.carbon.2017.06.017
53. Sneka S., Ananthi V, Sivakumar G (2026) Synthesis and characterization of $Bi_4Ti_3O_{12}$ based supercapacitor for energy storage applications. MRS Advances 11:1080–1087.https://doi.org/10.1557/s43580-026-01726-0
54. Chen K, Hu R, Feng X, Xie K, Li Y, Gu H (2013) $Bi_4Ti_3O_{12}/TiO_2$ heterostructure: Synthesis, characterization and enhanced photocatalytic activity. Ceramics International 39.8:9109-9114.http://dx.doi.org/10.1016/j.ceramint.2013.05.007
55. Hou J, Yang C, Wang Z, Ji Q, Li Y, Huang G, Jiao S, Zhu H (2013) Graphitic carbon nitride prepared by heat-treatment of melamine in air with highly enhanced photocatalytic activity under visible light, Appl. Catal B 579:142–143. http://dx.doi.org/10.1016/j.apcatb.2013.05.078
56. Liu Z, Zhao Z.G, Miyauchi M (2009) Efficient Visible Light Active $CaFe_2O/WO_3$ Based Composite Photocatalysts: Effect of Interfacial Modification, J. Phys. Chem. C 11317132. https://doi.org/10.1021/jp906195f
57. Zhu H, Yang B, Xu J, Fu Z, Wen M, Guo T, Fu S, Zuo J, Zhang S (2009) Construction of ternary CdS–Au–TiO_2 hollow nanorod arrays for a solid-state Z-scheme photocatalytic system. Appl. Catal. B 90:463. doi:10.1016/j.apcatb.2009.04.006
58. Wang X, Li S, Ma Y, Yu H, Yu J (2011) $H_2WO_4{\cdot}H_2O$/Ag/AgCl Composite Nanoplates: A Plasmonic Z-Scheme Visible-Light Photocatalyst. J. Phys. Chem. C 115 14648.https://doi.org/10.1021/jp2037476
59. Benbrika C , Menasra H, Kularkar A, Smaili L, Sbaihi A (2024) Enhanced photocatalytic degradation of rhodamine B using Fe/Ba-doped Bi4Ti3O12 nanostructures: Mechanism and performance evaluation.Journal of physics and chemistry of solids 184:111702. https://doi.org/10.1016/j.jpcs.2023.111702